remote sensing

MDPI

Article

Time-Dependent Systematic Biases in Inferring Ice Cloud Properties from Geostationary Satellite Observations

Dongchen Li [1,*], Masanori Saito [1] and Ping Yang [1,2,3]

[1] Department of Atmospheric Sciences, Texas A&M University, College Station, TX 77843, USA
[2] Department of Oceanography, Texas A&M University, College Station, TX 77843, USA
[3] Department of Physics & Astronomy, Texas A&M University, College Station, TX 77843, USA
* Correspondence: lidc@tamu.edu

Abstract: Geostationary satellite-based remote sensing is a powerful tool to observe and understand the spatiotemporal variation of cloud optical-microphysical properties and their climatologies. Solar reflectances measured from the Advanced Baseline Imager (ABI) instruments aboard Geostationary Operational Environmental Satellites 16 and 17 correspond to different spatial pixel resolutions, from 0.5 km in a visible band, up to 2 km in infrared bands. For multi-band retrievals of cloud properties, reflectances with finer spatial resolution need to be resampled (averaged or sub-sampled) to match the coarsest resolution. Averaging all small pixels within a larger pixel footprint is more accurate but computationally demanding when the data volume is large. Thus, NOAA operational cloud products incorporate sub-sampling (selecting one high-resolution pixel) to resample the reflectance data, which could cause potential retrieval biases. In this study, we examine various error sources of retrieval biases of cloud optical thickness (COT) and cloud effective radius (CER) caused by sub-sampling, including the solar zenith angle, viewing zenith angle, pixel resolutions, and cloud types. CER retrievals from ice clouds based on sub-sampling have larger biases and uncertainties than COT retrievals. The relative error compared to pixel averaging is positive for clouds that have small COT or CER, and negative for clouds that have large COT or CER. The relative error of COT decreases as the pixel resolution becomes coarser. The COT retrieval biases are attributed mainly to cirrus and cirrostratus clouds, while the largest biases of CER retrievals are associated with cirrus clouds.

Keywords: ice clouds; resampling; GOES-16/17; pixel resolution; diurnal variation; remote sensing

Citation: Li, D.; Saito, M.; Yang, P. Time-Dependent Systematic Biases in Inferring Ice Cloud Properties from Geostationary Satellite Observations. *Remote Sens.* **2023**, *15*, 855. https://doi.org/10.3390/rs15030855

Academic Editor: Anthony J. Baran

Received: 23 November 2022
Revised: 21 January 2023
Accepted: 1 February 2023
Published: 3 February 2023

1. Introduction

Ice clouds cover approximately 20% of the globe and are recognized as critical factors regulating the global atmospheric energy budget, and thereby influencing the climate system [1–3]. The optical and microphysical properties of ice clouds vary greatly with time and location [4,5], and the current understanding of their spatial and temporal variations is still limited. These variations contribute significantly to the uncertainty of cloud radiative forcing in climate models [6,7]. Sun-synchronized polar-orbiting satellites in conjunction with remote sensing techniques can estimate key cloud properties, such as cloud droplet/particle effective radius (CER), cloud optical thickness (COT), cloud top height (CTH), and cloud thermodynamic phase, from passive radiometric measurements (e.g., [8]), active sensor measurements such as radar (e.g., [9]), or active-passive combined measurements (e.g., [10]). However, polar-orbiting satellite observations have, significantly, a low temporal resolution (usually viewing a location twice a day), making it difficult to depict diurnal variations of cloud properties. Geostationary satellite observations with remote sensing techniques allow the monitoring of regional cloud properties with a high temporal resolution [11].

A geostationary satellite orbits over the equator at a fixed altitude (about 35,880 km) and is able to observe a specific region continuously. Such satellites, including Himawari-8,

Meteosat-8–11, and Fengyun-4, are used for scientific research, daily weather forecasting, and long-term climate monitoring. In particular, the Geostationary Operational Environmental Satellites (GOES) operated by NOAA and NASA play a pivotal role in monitoring cloud optical and microphysical properties over North and South America, and the Eastern Pacific and Atlantic Oceans. The Advanced Baseline Imager (ABI) instrument aboard GOES-16/17 is a state-of-the-art 16 band (or channel) radiometer, with two visible, four near-infrared, and ten infrared channels, providing high temporal resolution from 30 s to 15 min, and spatial resolution from 0.5 to 2 km [12]. It provides 37 operational products that have been validated and utilized in many different research projects [13,14]. In particular, COT and CER are key parameters to understand cloud radiative forcing and aerosol-cloud interactions [15,16], and these cloud properties can be inferred from the top of the atmosphere (TOA) reflectance data at visible and near-infrared (VIS-NIR) wavelengths based on the bi-spectral method [17]. Reflectance data in ABI bands 2 (0.64 μm) and 6 (2.24 μm) are applied to retrieve COT and CER.

However, the pixel resolution of the band 2 reflectance data is 0.5 km at nadir, which is finer than the 2-km resolution of band 6. To provide operational cloud products based on the bi-spectral method, the band 2 reflectance data need to be resampled, or converted in spatial resolution from a finer 0.5-km to a coarser 2-km resolution. The simplest resampling approach is sub-sampling [18] by choosing a pixel within a 2-km super-pixel domain to represent the 2-km domain. The most accurate method is pixel-averaging that averages all 16 pixels in the 2-km super-pixel domain. Due to the large volume of GOES-16/17 reflectance data, the current operational cloud products rely on sub-sampling. This simplified resampling process could induce retrieval biases and uncertainties associated with clouds and geometric characteristics, because the chosen 0.5-km pixel covers only a part of the larger 2-km pixel.

Previous studies have quantitatively investigated the factors that can cause uncertainties and biases in the retrieval results. Coakley et al. showed that the retrieved cloud properties, including COT, CTH, liquid water path, and column droplet number concentrations, are typically underestimated due to the assumption of overcast pixels, although a majority of those pixels are partly cloudy [19]. If the solar zenith angle (SZA) is large, COT retrieval results are usually overestimated [20]. Zhang et al. find that the impact of the overcast assumption on COT is caused only by the subpixel variation of VIS/NIR band reflectance, and the COT retrieved from coarse-resolution reflectance is generally smaller than that retrieved from high-resolution data due to the homogeneous subpixel assumption [21]. They developed a mathematical framework that can accurately simulate the bias caused by the subpixel variation of cloud reflectances. Werner et al. further validated the result derived from this framework using high-resolution reflectance observations from the Advanced Spaceborne Thermal Emission and Reflection Radiometer [22]. Kahn et al. found that COT retrieved from the Atmospheric Infrared Sounder (AIRS) and the Moderate Resolution Imaging Spectroradiometer (MODIS) both have large uncertainties in a heterogeneous ice cloud [23]. The highest correlation of COT retrieved from these two instruments appears in single-layered horizontally homogeneous clouds, which suggests that horizontal cloud inhomogeneity and vertical cloud structure are two important factors reducing the accuracy of the cloud optical property retrievals. In addition, the SZA and pixel resolution have substantial impacts on the reflectance received by the satellite, which affects the cloud property retrieval and increases its uncertainty [7,24–26], which could produce further errors during the resampling process.

The aforementioned studies have pointed out that partial cloud coverage, subpixel inhomogeneity, cloud structure, SZA, and pixel resolution can potentially contribute to the retrieval biases, and the biases can be amplified by the resampling process. However, the potential retrieval biases induced by the resampling process, and its dependence on different factors, are not well understood. In this study, we investigate the impact of different spatial resolutions of the GOES-17 reflectance data over ocean on ice cloud COT and CER retrievals, and examine the time-dependent relative error of the retrieval results

associated with the sub-sampling method, with a particular focus on the error dependence on SZA, pixel resolution, and cloud types. Section 2 describes the data and criteria, methods for the resampling process, and geometry calculations. Section 3 shows the results. Section 4 concisely summarizes and discusses the major conclusions derived from this study.

2. Data and Methodology

2.1. Data and Pixel Selection Criteria

This study uses GOES-17 ABI full-disk operational products, including cloud top pressure (CTP, 10 × 10 km at nadir), cloud top phase (2 × 2 km), and reflectances in Band 2 (0.5 × 0.5 km), 3 (1 × 1 km), and 6 (2 × 2 km) during the daytime [18,27,28]. The data cover latitudes from 81.3282° South to 81.3282° North, and longitudes from 141.9005° East to 55.9005° West. We analyze two days of data, 20 March 2019 and 23 September 2019, i.e. the spring and fall equinoxes, when the sun is directly above the equator, hence there are more pixels that have the same local solar time to investigate the time dependence of the retrieval biases that are caused by the resampling process. To make the resolution consistent with the resampled reflectance data and cloud top phase data, linear interpolation is used to change the resolution of the CTP data from 10 km to 2 km. As discussed in Section 2.2, the reflectance data are resampled to be prepared for the retrievals.

For a retrieval procedure, we use the MODIS Collection 6 (C6) bulk ice optical property model [8,29], calculated from the single-scattering properties of severely-roughened eight column aggregate particles [30], weighted by particle size distributions over particle sizes from 2–10,000 μm [31]. We use an adding-doubling radiative transfer model [32] to construct a look up table (LUT) of ice cloud reflectances for various combinations of COT and CER. We then apply a reliable VIS-NIR retrieval system developed to retrieve COT and CER based on optimal estimation, that obtains an optimal solution by minimizing a cost function [33]. The range of retrieved values for state vectors (COT, CER) is 0.1 to 150 for COT, and 1 μm to 100 μm for CER.

To improve the quality and accuracy of the retrieval results, we use pixels that satisfy the criteria listed in Table 1. The GOES-17 cloud top phase product is used to select pixels that are identified as covered by ice clouds. The cloud top phase product is derived based on the GOES-17 cloud mask product, which is retrieved from sub-sampled band 2 reflectance data [34]. We use pixels over oceans only, as the radiative contribution from land is not negligible due to a large surface albedo [35]. The retrieval failure rate (see Section 3.1) can be enhanced when the pixel has a large SZA or viewing zenith angle (VZA), or is strongly influenced by sunglint [36], so we limit the SZA and VZA to less than 60° and 80°, respectively. The sunglint angle is defined as the angle between the line from the viewing pixel to the satellite and the reflected sun ray from that pixel, and is calculated by:

$$\alpha = 180 \times [1 - \frac{\cos^{-1}(-\cos\theta\cos\theta_e - \sqrt{1-\cos\theta^2}\sqrt{1-\cos\theta_e{}^2}\cos\eta_R)}{\pi}] \quad (1)$$

where α is sunglint angle, θ is SZA, θ_e is VZA, and η_R is relative azimuth angle (RAA; all angles are stated in degrees in this paper, but computer trigonometric calculations must be performed in radians and then converted to degrees). We filter out pixels that have $\alpha < 30°$ to reduce sunglint effects [37]. This study analyzes only pixels for which the retrieval produces an optimal solution, which account for 79% of the total pixels that meet the criteria mentioned above.

To understand the contributions of different cloud types to the relative error of the retrieval results, we use the International Satellite Cloud Climatology Project (ISCCP) cloud types diagram to approximately classify different cloud types based on CTP and COT [38]. Table 2 shows the criteria from ISCCP that are used to distinguish different types of high clouds (Cirrus, Cirrostratus, Cumulonimbus).

Table 1. Pixel data acceptance criteria.

Variable Name	Threshold for Acceptance
Cloud top phase	Ice
SZA	<60°
VZA	<80°
Surface type mask	Ocean
Day/Night flag	Day
Sunglint angle	>30°

Table 2. ISCCP cloud classification for high cloud types.

	Cloud Types	COT	CTP
High Clouds	Cirrus	<3.6	0–440 hpa
	Cirrostratus	3.6–23	0–440 hpa
	Cumulonimbus	23–150	0–440 hpa

2.2. Resampling Methods

The spatial resolution of TOA reflectance observed by GOES-17 is 0.5 km for band 2 (0.64 μm), 1 km for band 3 (0.86 μm), and 2 km for band 6 (2.24 μm). It is necessary to resample the reflectance data from the smallest pixel (0.5 or 1 km) in each band to a 2-km pixel to make the spatial resolution of the reflectance consistent among the bands for retrievals. We use two operational resampling algorithms described in GOES-R ABI Algorithm Theoretical Basis Document for Cloud and Moisture Imagery Product (CMIP) [18]. The default method is sub-sampling, which is used to resample the reflectance from the finest resolution. The sub-sampling applied to 0.5-km resolution data selects one pixel among 16 pixels (with 1-km data, one pixel is selected among 4 pixels) to represent the 2-km pixel. This method is computationally efficient and does not involve additional mathematical operations. However, the accuracy of the reflectance could be affected by several factors, which will be further discussed in the following sections. The second method is to average all smaller pixels in the 2-km pixel to resample the data. This method is more accurate, and it can improve the signal-to-noise ratio, but it is computationally demanding when applied for operational processing.

To have a more comprehensive understanding of the sub-sampling impact, we designed three experiments (illustrated in Figure 1) to process the reflectance data in band 2, with a 0.5-km resolution, compared to the 2-km band 6 pixel. The first experiment, Case A, uses the pixel-averaging method to average all 16 0.5-km pixels in the 2-km pixel. This case is used as a benchmark, since pixel-averaging is equivalent to replacing the high-resolution sensor with a 2-km resolution sensor. Case B uses the pixel-averaging method to average four 0.5-km pixels into a 1-km pixel, and then uses the sub-sampling method (selecting that constructed 1-km pixel) from 1 km to 2 km. This case can be used to analyze the impact of data resolution on the sub-sampling result. The last experiment is Case C, which only uses the sub-sampling method (selecting one 0.5-km pixel) to resample the data from 0.5 to 2 km. Using these three cases for analysis, we can have a rigorous assessment on the impact of the pixel resampling method used. Figure 1 illustrates the three experiments (Cases A–C), showing a potential geographical bias by selecting 0.5 or 1-km pixels away from the center of the 2-km pixel, but the geographical bias is negligible in 2-km because the location error is <1 km. Instead, the COT retrieval bias in this paper occurs largely because partial cloud cover, or other inhomogeneities, in a 2-km area cause a 0.5 or 1-km pixel to most frequently underrepresent the 2-km average COT, as discussed later. Since the effective pixel resolution varies depending on the geolocation of the pixels, hereafter we often name a 0.5- or 1-km sub-sampled pixel as a "sub-pixel", and the corresponding 2-km pixel as a "super-pixel".

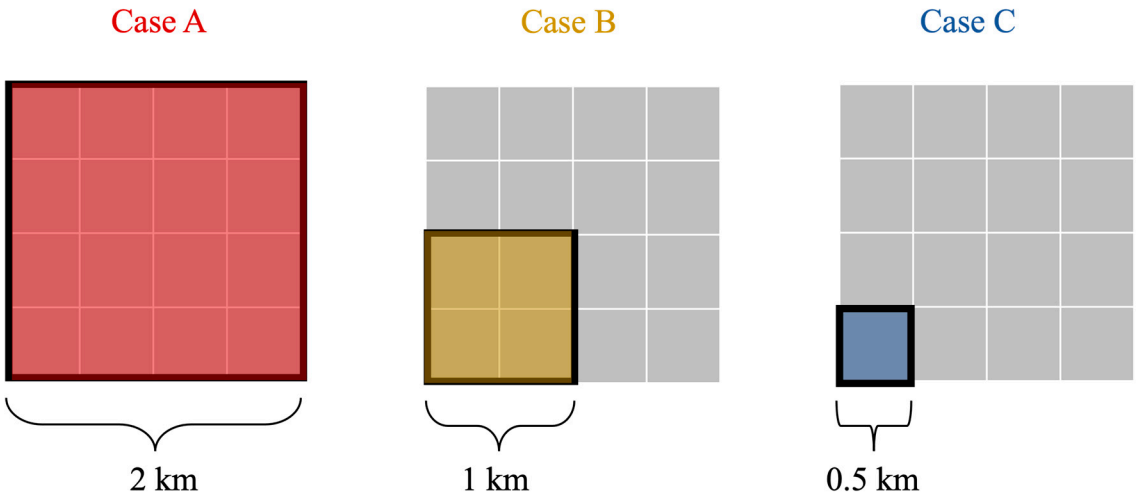

Figure 1. Illustration of three resampling cases. Case A represents averaging all 0.5-km pixels in the 2-km resolution pixel to represent the reflectance in the whole 2-km pixel. Case B represents averaging a block of 4 0.5-km sub-pixels to represent the reflectance in a 1-km pixel, and using that average as the sub-sampled 1-km pixel to represent the 2-km super-pixel reflectance. Case C uses the reflectance in one 0.5-km sub-pixel to represent the reflectance in the whole 2-km super-pixel.

2.3. Resampling Methods

The retrievals are affected by sun-view geometries such as SZA, VZA, and relative azimuthal angle (RAA). Figure 2 shows an example of the GOES-17 sun-view geometry for a pixel. The SZA is defined as the angle between the local zenith and the line of sight from that point to the sun. It can be calculated with spherical trigonometry using:

$$\cos\theta = \sin\varphi \sin\delta + \cos\varphi \cos\delta \cos h \tag{2}$$

where θ is SZA; φ is the local latitude at the observation point; δ is the declination of the Sun in the ecliptic; and h is the hour angle. Both δ and h are a function of the local time (LT) with a 24-h clock and the day of the year. The VZA θ_e is the angle between the line from an observational point on Earth's surface to a satellite sensor and the line from the same observational point perpendicular to Earth's horizontal surface. For simplicity, Earth is assumed to be a sphere. The VZA can be calculated using the following equations:

$$\theta_e = \frac{180}{\pi} \sin^{-1}\left(\frac{H_{eq} \sin(\beta)}{\sqrt{{H_{eq}}^2 + {r_{eq}}^2 - 2H_{eq} r_{eq} \cos(\beta)}}\right) \tag{3}$$

$$\beta = \frac{180}{\pi} \cos^{-1}\left(\cos(\varphi - \varphi_0)\cos(\lambda - \lambda_0)\right) \tag{4}$$

where φ_0 and λ_0 are satellite subpoint latitude and longitude on Earth (0° and −137.2° for GOES-17), φ and λ are the latitude and longitude of the observation point on Earth, and β is the geocentric angle (the angle along the great circle from the subpoint to the observation point). H_{eq} and r_{eq} are the satellite height from the center of Earth and the length of the semi-major axis of Earth (radius at the equator), which are set to 42,164.16 km and 6378.137 km for GOES-17. The RAA is defined as the relative angle between the sun and the satellite direction. In this case, the viewing azimuth angle (VAA) and solar azimuth angle (SAA) should be first computed with the following two equations:

$$\cos\ \eta_s = \frac{\sin\varphi_0 - \sin\varphi\cos\beta}{\cos\varphi\sin\beta} \tag{5}$$

$$\cos\eta_0 = \frac{\sin\delta - \sin\varphi\cos\theta}{\cos\varphi\sin\theta} \tag{6}$$

where η_s is VAA, and η_0 is SAA. To derive η_s and η_0, the arccosine function is applied to Equations (5) and (6). Due to the nonlinearity of the cosine function, an accurate RAA calculation requires a correction to SAA and VAA. The hour angle in LT is defined as follows: At solar noon the hour angle is 0°, with LT before solar noon expressed as negative degrees. For example, at 10:30 LT, the hour angle is −22.5° (15° per hour times 1.5 h before noon). We correct SAA (η_0) using:

$$\begin{cases} \eta_0 = 360 - \eta_0 & h > 0 \\ \eta_0 = \eta_0 & h \leq 0 \end{cases} \tag{7}$$

Since the detector is a geostationary satellite, the subpoint of the satellite does not change with time. We can use the longitude of the satellite subpoint to correct VAA (η_s):

$$\begin{cases} \eta_s = 360 - \eta_s & \lambda > \lambda_0 \\ \eta_s = \eta_s & \lambda \leq \lambda_0 \end{cases} \tag{8}$$

After the corrected SAA and VAA are derived, the equations below can be used to calculate the relative azimuth angle RAA (η_R):

$$\Delta\eta = \eta_0 - \eta_s, \tag{9}$$

$$\Delta\eta = \begin{cases} \Delta\eta \geq 360°, & \Delta\eta - 360 \\ 0° \leq \Delta\eta < 360°, & \Delta\eta, \\ \Delta\eta < 0°, & \Delta\eta + 360 \end{cases} \tag{10}$$

$$\eta_R = |\Delta\eta - 90|. \tag{11}$$

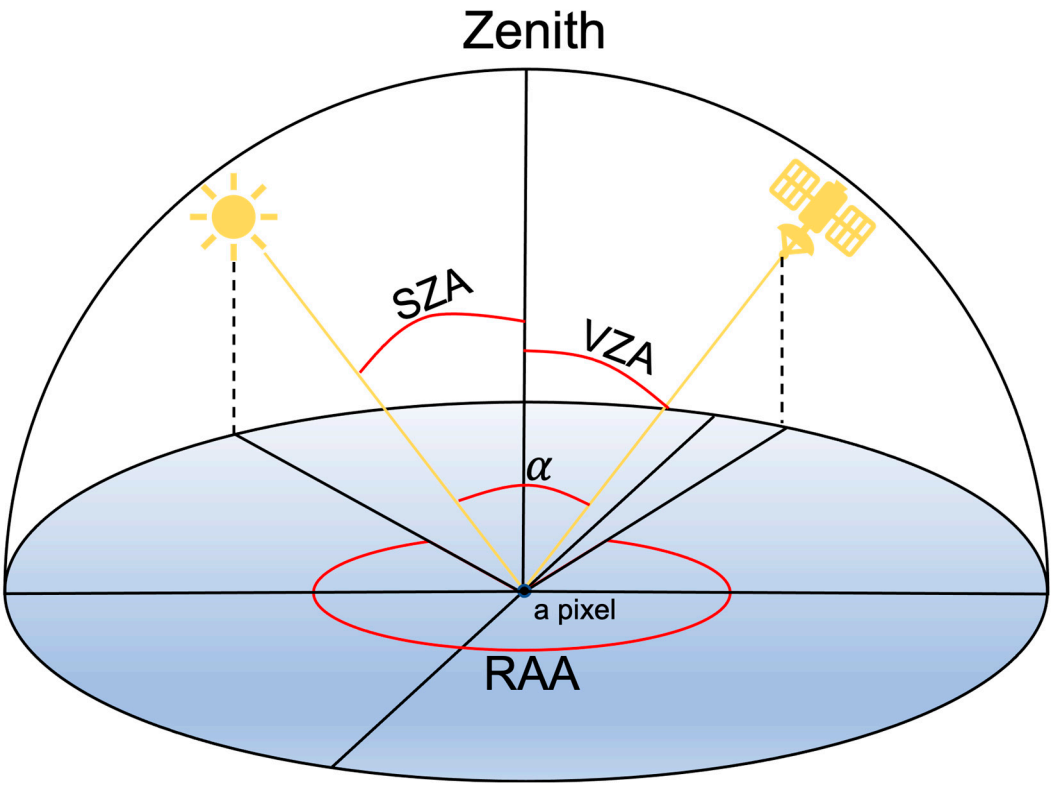

Figure 2. Schematic Diagram of the GOES-17 sun-view geometry.

2.4. Off-Nadir Pixel Resolution

The actual pixel resolution at an off-nadir location is coarser than at the nadir location, as it is stretched due to the curvature of Earth and the slant view (or the VZA). The effective pixel resolution is defined as the square root of the projected pixel area. For simplicity, we assume that a pixel at the subpoint on the surface is a circle with a radius (r_1) that gives the area of the circle consistent with the original super-pixel area A_p, which is 4 km^2 in this study. A projected super-pixel at any off-nadir location is almost exactly an ellipse based on this assumption. The r_1 can be derived from:

$$r_{1=}\sqrt{\frac{A_p}{\pi}}. \tag{12}$$

To derive the effective super-pixel resolution, first account for the distance effect, that the super-pixel size will get larger as the distance becomes longer. The distance L between a super-pixel of interest and the satellite is:

$$L = \sqrt{{r_{eq}}^2 + (r_{eq} + H)^2 - 2r_{eq}(r_{eq} + H)\cos(\beta)}, \tag{13}$$

where H is the distance between the satellite and its sub-point super-pixel. The angular location of the GOES-17 sub-point (nadir point) is (0°, −137.1999969°). The ratio of H to L should equal the ratio of r_1 to the enlarged super-pixel radius (r_2). Therefore, we can get the enlarged super-pixel radius (perpendicular to the satellite viewing path) through this relationship:

$$r_2 = \frac{L}{H}r_1. \tag{14}$$

Note that r_2 is also the semi-minor axis of the projected super-pixel ellipse on the surface. The second (VZA) effect is accounted for by deriving the projected super-pixel semi-major axis (r_3) using the trigonometric relationship between the VZA and enlarged super-pixel size:

$$r_3 = \frac{r_2}{\cos\theta_e}. \tag{15}$$

The projected super-pixel area is computed using the elliptic area formula. The effective super-pixel resolution (r_p) is defined as:

$$r_p = \sqrt{\pi r_1 r_3}. \tag{16}$$

Since the line between the viewing point and satellite is almost horizontal to the surface when the VZA is close to 90°, the effective super-pixel resolution can be extremely large. We only accept and compute the effective super-pixel resolution if VZA < 80°. Figure 3 shows the distribution of the effective super-pixel resolution. The resampling effect on retrievals such as COT could vary with different effective super-pixel resolutions. Therefore, the impact of the effective super-pixel resolution will be further discussed in the following sections.

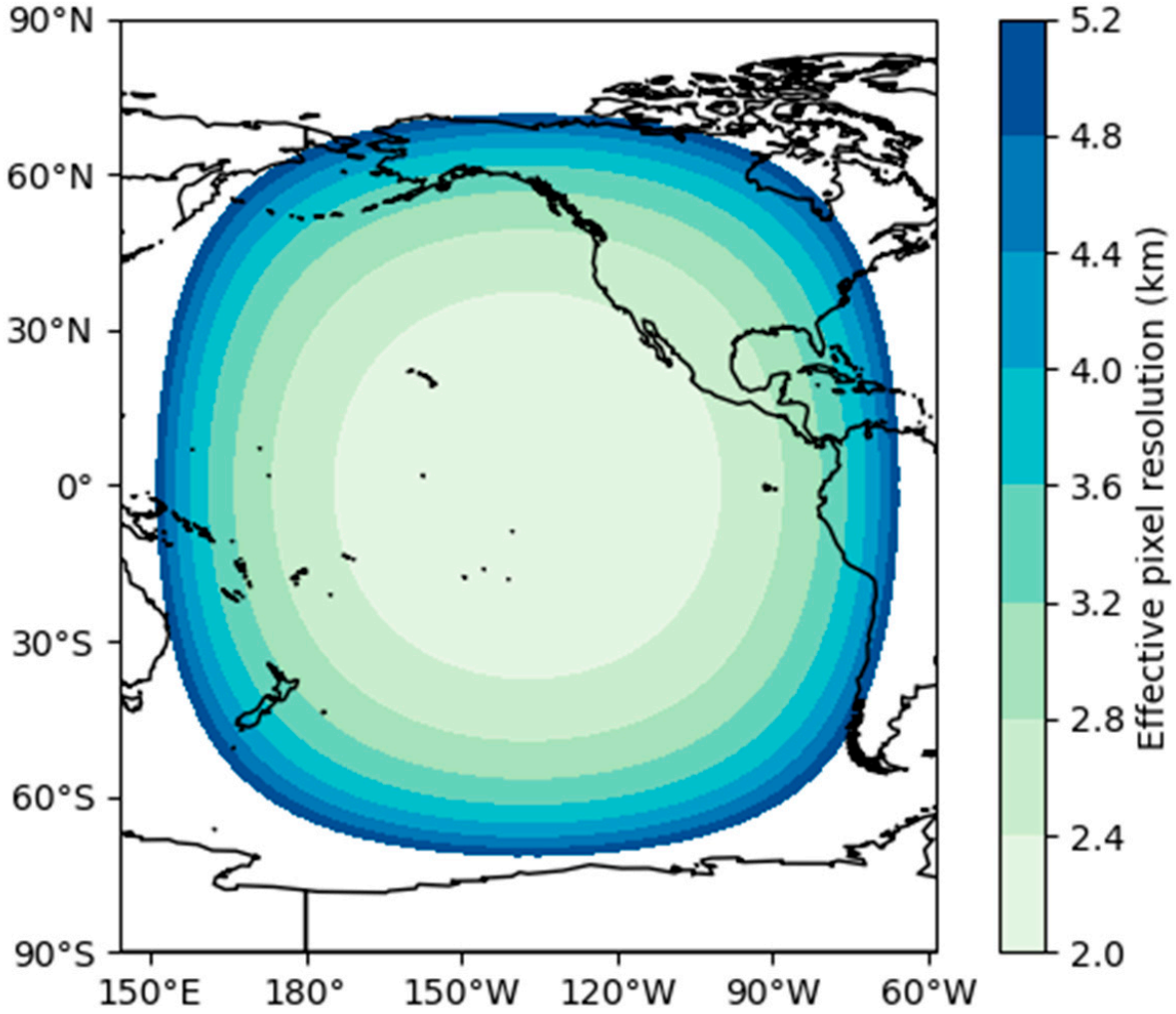

Figure 3. The distribution of projected effective super-pixel resolution in a GOES-17 ABI full-disk image.

3. Results

3.1. Comparison of COT and CER Retrievals among the Resampling Methods

We explore the principle that the retrieval results vary with a different sub-sampled band 2 reflectance, plotted on the Nakajima–King diagram shown in Figure 4. The relative error is defined as the relative difference of the retrieval results from Case B or C minus Case A. Figure 4 schematically shows the changes in the COT and CER retrieval results when the reflectance in Case B or C is larger or smaller than that in Case A. The circular marks and lines in yellow represent the COT and CER retrieval results in Case A, which is considered as the benchmark in this study. When the reflectance in Case B or C is larger (smaller) than the counterpart in Case A, which is illustrated in red (green), the retrieval results in Case B or C tend to be larger (smaller) than in Case A, providing a positive (negative) relative error. However, distribution of the relative error will be skewed, due to the boundary values of the state vectors set in the retrieval system, if the retrieval results are close to the boundary value. For example, if the retrieved CER or COT value in Case A is so small that it is close to the lower boundary value, the case that has a negative relative error will have a smaller CER or COT value in Case B or C than that in Case A. In this case, the retrieval result may be outside the predefined boundary, which will be counted as a non-optimal solution or a failed retrieval. Therefore, the relative error will almost always be positive in this case, or else the retrieval will not be successful.

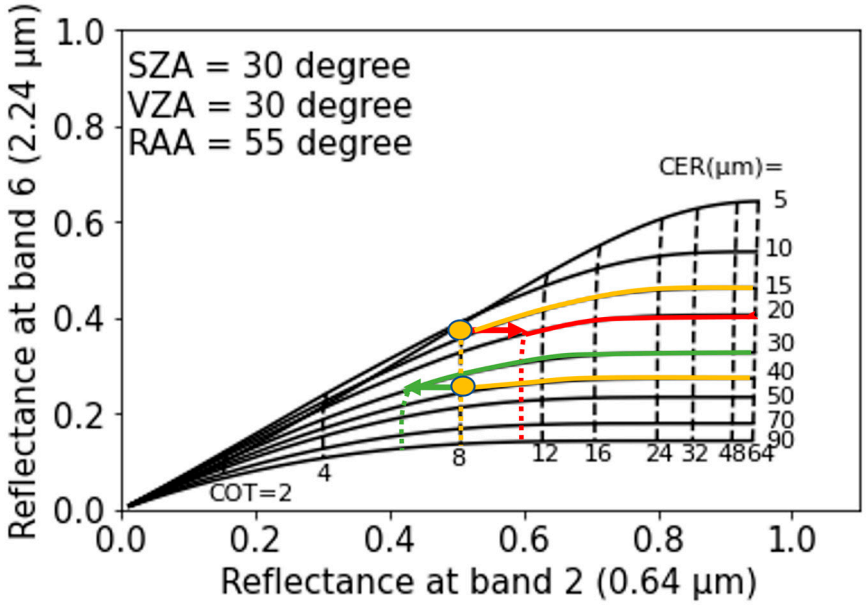

Figure 4. Nakajima–King schematic diagram based on the MODIS collection 6 ice particle model. The circular marks and lines in yellow correspond to the retrieval results from Case A, which is considered to be the benchmark. The red and green arrows indicate the circumstances that the reflectances from Case B or C are larger or smaller than the reflectance in Case A, and the lines in red and green stand for the corresponding COT and CER retrieval results, respectively.

Figure 5 shows the COT and CER retrieval biases associated with the resampling process from ice clouds in Cases B and C. The shaded regions show the weighted standard deviation of relative retrieval errors for each resampling case. From Figure 5a,b, the standard deviation for Case C is larger than that for Case B in both the COT and CER retrieval cases. This is reasonable, because using four 0.5-km sub-pixels to represent the average of 16 pixels has a smaller error than using one sub-pixel. Averaging the sub-pixels within a super-pixel can reduce cloud heterogeneity effects that can greatly bias the retrieved COT, reaching up to −70%, −50%, or +40% for backward, nadir and forward viewing directions, respectively [39]. In Figure 5, variations of the relative errors of the COT and CER have a similar trend, that the relative error is positive when the COT or CER value is small, and it becomes negative when the COT or CER value is large. Based on the discussion of Figure 4, this is partly due to the retrieval boundary limitation. The other possible reasons will be discussed in detail below.

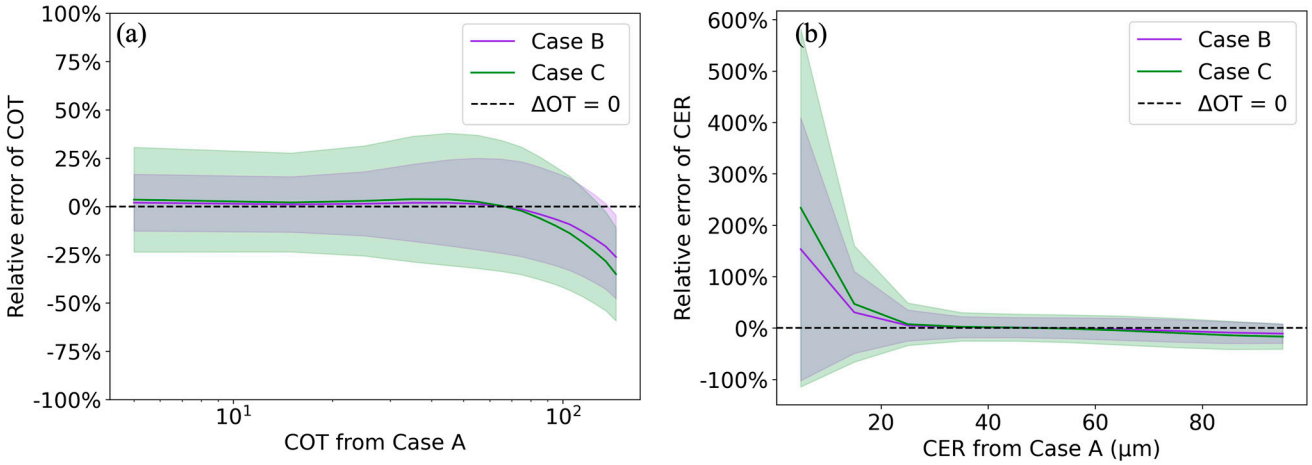

Figure 5. Relative errors of Case B and Case C as a function of (**a**) COT or (**b**) CER retrieved from pixel-averaging as in Case A. The shaded regions show ±1 weighted standard deviation.

For the COT retrievals shown in Figure 5a, the mean relative error is positive for optically thin cases, because the reflectance is more sensitive to medium and smaller COT values [40], hence the mean COT value retrieved in Case B or Case C is larger than the average of the COT value in Case A. In addition to the nonlinear relationship between the reflectance and the COT, the partial cloud coverage effect can also contribute to this positive relative error, which will be discussed in the following sections. However, the mean relative error is negative for optically thick cloud cases, which could be due to small spatial scales of clouds, such as deep convective clouds [41]. For example, the reflectance from an isolated deep convective cloud, or from clouds that have a small horizontal spatial scale, might not be captured by sub-sampling, but it is considered in the pixel-averaging method, which makes the retrieved COT value become larger in Case A. This could be a major reason for the negative COT biases in optically thick cloud cases.

Comparing Figure 5a,b, the average value and weighted standard deviation of the CER relative error is much higher than that of the COT relative error. The maximum value of the mean CER relative error is about 250% for the smallest particles (1 μm) in Case C, decreases to near zero when the Case A CER is between about 25 and 60 μm, and the relative error is negative for larger CER values. Figure 6 shows the distribution of COT in different CER intervals. The CER relative error at CER is <20 μm and mainly comes from optically thin clouds (COT < 5) that have positive COT relative errors. Because of the nonorthogonal correlation between COT and CER, the relative error of CER is positive. Since the CER is more sensitive to changes in band 2 caused by sub-sampling, as the COT is small, the scale of the relative error of the CER is much larger than that of the COT. For example, if the CER is so small that is close to the lower boundary limit (1 μm), the COT will be less than 5, as discussed above, and the nonorthogonal correlation between COT and CER will be extremely strong, as illustrated in the lower-left portion of Figure 4. In this case, a slight bias in the COT retrieval results, which is caused by the sub-sampling method, can lead to a significant bias in the CER retrieval. The COT becomes relatively larger when the CER ranges from 20 to 60 μm, in which case COT and CER are almost orthogonal. In this case, changes in COT are nearly independent from CER, and the relative error of CER is close to 0 in this interval. Although the COT is still small for clouds with CER > 60 μm, the relative error of CER is negative due to the boundary limitation set in the retrieval system.

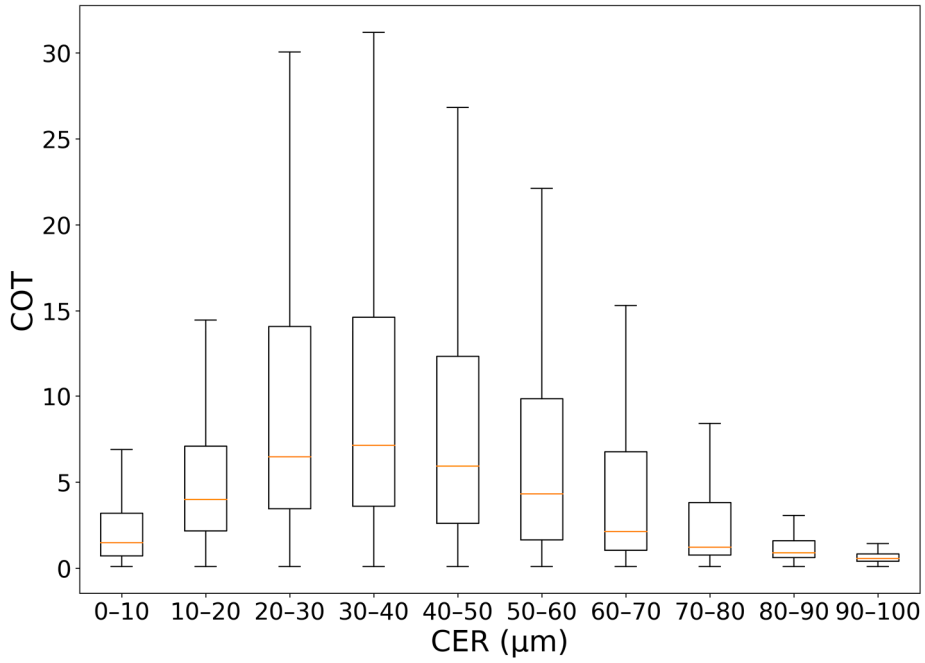

Figure 6. Box plot representing COT in various CER intervals based on Case A retrievals.

3.2. Impact of Effective Pixel Resolutions

We investigate the relative errors of the COT and CER dependence on the effective pixel resolution and SZA for three types of high clouds, which we classified based on the criteria in Table 2. In total, 70,888,651 pixels are identified as covered by cirrus clouds, 119,701,320 pixels are identified as covered by cirrostratus clouds, and 22,426,280 pixels are identified as covered by cumulonimbus clouds. Since the CTP product only covers a part of the GOES-17 full disk image, we focus on the region that has an effective pixel resolution less than 3.8 km. Figure 7a–c, show that the majority of the COT's relative error is positive, except for the upper left corner of Figure 7a, which has small negative biases when the effective pixel resolution is larger than 3.2 km and SZA is smaller than 20°. As the NOAA Case B and C operational products are based on sub-sampling of higher-resolution sub-pixels [18], a sub-pixel is considered overcast even if it is in a partly cloudy super-pixel, but the reflectance of a partly cloudy super-pixel is systematically smaller than that of a cloudy sub-pixel due to clear sky contamination. In consequence, as the COT retrieval is performed based on the overcast assumption, the retrieved COTs in Case C and Case B can be systematically larger than those in Case A. Therefore, the relative error of the COT is typically positive.

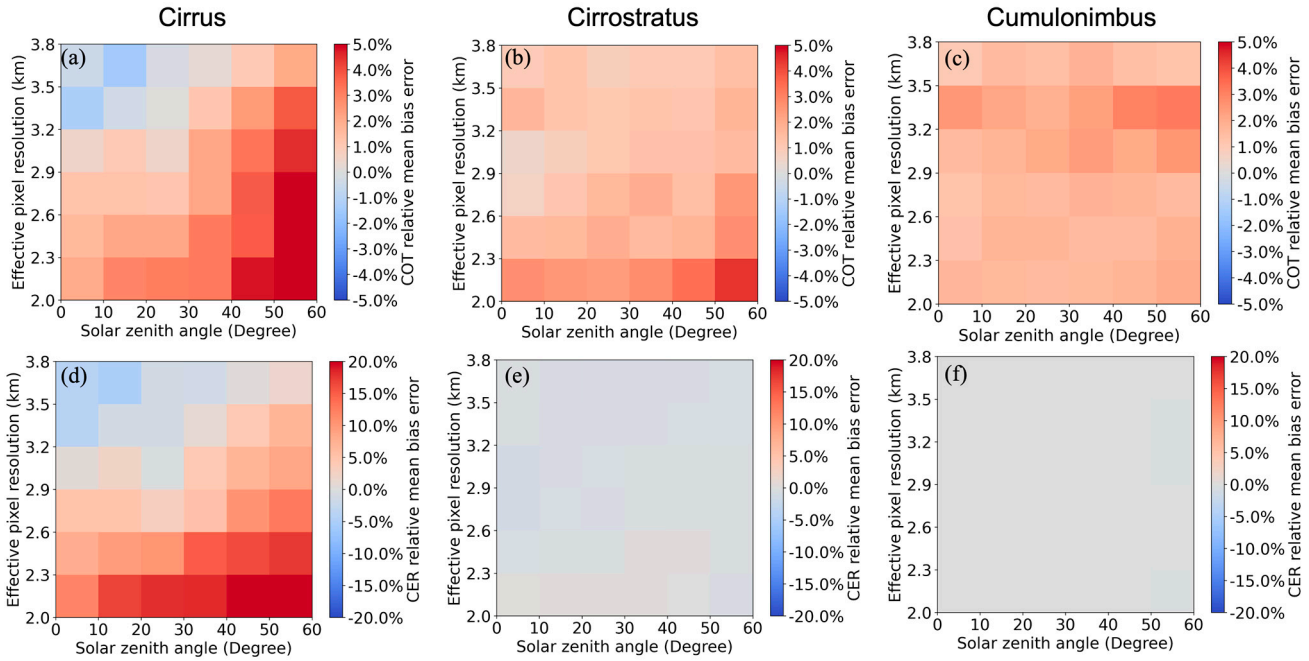

Figure 7. 2-D histogram of the COT and CER retrieval relative mean bias errors for Cirrus (**a**,**d**), Cirrostratus (**b**,**e**), and Cumulonimbus (**c**,**f**) as a function of SZA (x-axis) and effective pixel resolution (y-axis). The colors depict the relative mean bias error, defined as the difference of the retrieved COT or CER of Case C minus Case A.

In Figure 7a–c, the relative error of the COT retrieved from cirrus and cirrostratus clouds decreases as the effective pixel resolution becomes coarser. Wood & Field found that the "near-global" cloud horizontal spatial scale varies according to a single power law distribution from <0.1 km to >1000 km, based on a composite of satellite and aircraft observations, and model simulations [42]. The number of clouds in a horizontal spatial scale size bin decreases as the size increases, indicating that the clouds typically have a horizontal spatial scale <1 km. As GOES-17 has a fine effective pixel resolution, the resolution of the sub-pixels is comparable to the median cloud horizontal spatial scale, which could enhance the impact of partial cloud coverage on the COT retrieval biases induced by sub-sampling. A super-pixel tends to have much more clear-sky area than a sub-pixel. As the effective pixel resolution becomes coarser, the larger sub-pixels and super-pixels will have higher

possibilities to be partly cloudy, due to the relatively small horizontal spatial scale of clouds. This causes the reflectance derived from Case C to become closer to the reflectance derived from Case A, and thereby the relative error of the COT retrievals decreases as the effective pixel resolution becomes coarser, as seen in Figure 7a–c. Iwabuchi & Hayasaka found that the variance of the retrieved COT largely depends on SZA, due to cloud three-dimensional (3D) radiative effects, which could be the reason for the increase of the COT relative error as SZA becomes larger [43]. In Figure 7a, the small negative relative error of COT that appears at effective pixel resolutions larger than 3.2 km and SZA less than 30° could be due to the boundary limitation and fewer valid pixels compared to other regions.

Figure 7a,d show a similar pattern, which indicates a good correlation between the relative error of COT and CER. This is due to the nonorthogonal correlation between COT and CER retrievals for Cirrus clouds that have small COTs. The relative error of the CER from Cirrostratus and Cumulonimbus clouds, shown in Figure 7e,f, remains near 0 regardless of the pixel resolution and SZA. Since the correlation between the COT and CER is close to orthogonal when the optical thickness is large, this verifies the previous point that changes in COT are nearly independent of CER in this case, thus the distribution of the COT relative error for these two types of clouds does not have much impact on the relative error of CER.

3.3. Temporal Dependence of the Relative Error with Different Types of Clouds

The GOES-17 satellite observations provide cloud properties with 15-min or less temporal resolution, and therefore can depict the diurnal variation of cloud properties. Figure 8 shows the LT-dependent COT and CER retrieval biases based on the results from Cases B and C. The relative errors of the COT retrievals are largest at 8:00 and 16:00 LT, and there is a broad minimum value of biases centered around 12:00 LT. In contrast to the COT retrievals, the relative errors of the CER retrievals show a larger variation with LT, with maxima at 8:00 and 16:00 LT. The trend of the COT relative error with LT is similar to that of the CER relative error due to a strong correlation between the relative errors of COT and CER. For both the COT and CER retrieval cases, the relative errors in Case B are smaller than those in Case C.

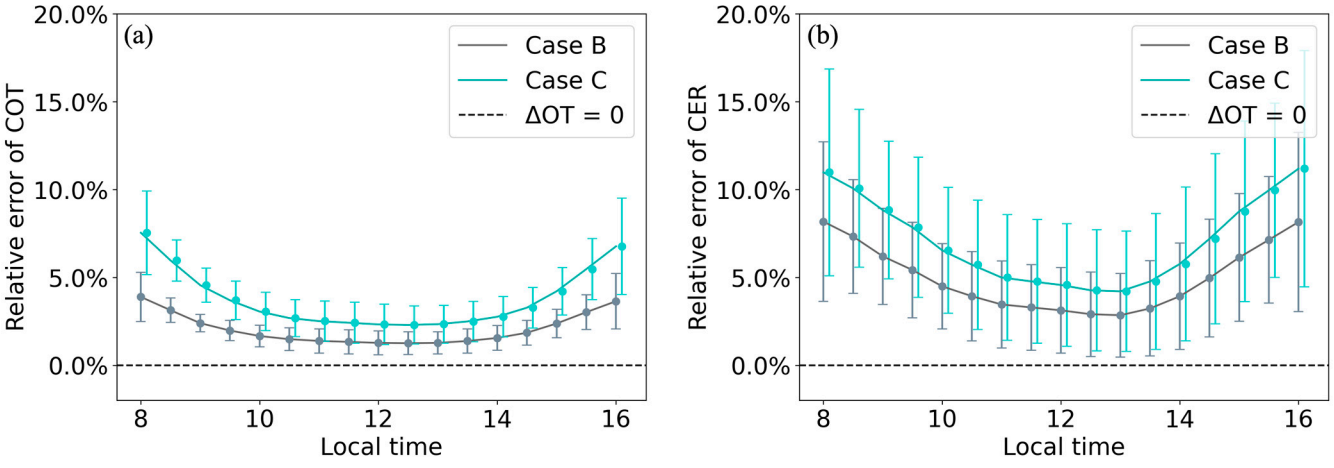

Figure 8. Relative error of (**a**) COT and (**b**) CER in Case B and Case C as a function of LT, based on GOES-17 retrievals for high clouds.

We use the ISCCP cloud classification criteria in Table 2 to stratify the temporal dependence of the COT retrieval errors with different high cloud types. Figure 9 shows the diurnal variation of the fraction of cloud types based on the GOES-17 CTP product, and COT retrievals of ice clouds from Case A, which are identified by using the GOES-17 cloud top phase product. From Figure 9, cirrostratus clouds dominate in the high cloud category, and cirrus is the second most abundant cloud type. Since the Nakajima–King

retrieval method has a limited sensitivity to optically thin clouds [44], the amount of cirrus clouds can be underestimated.

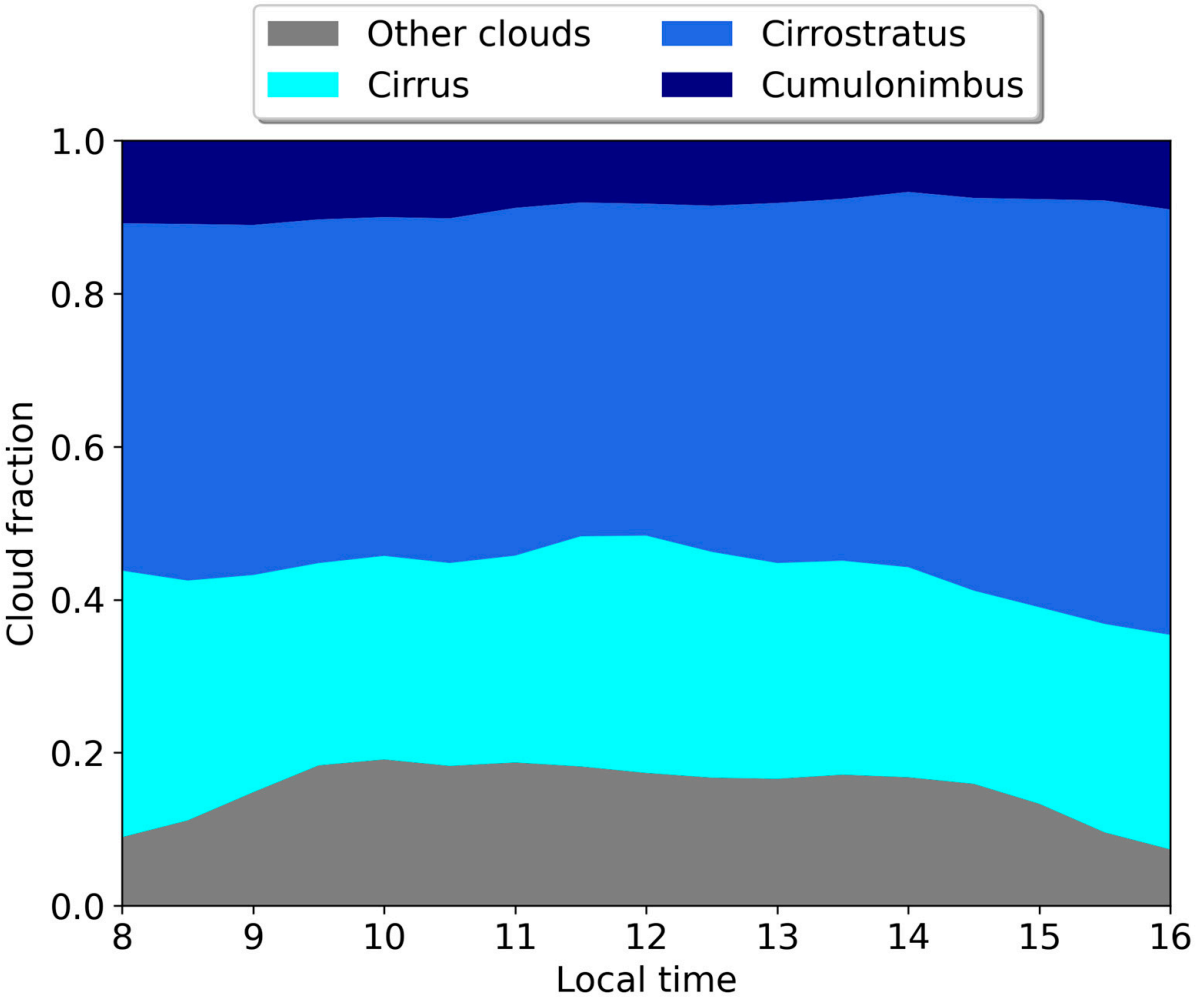

Figure 9. Cloud type fraction, based on ISCCP cloud classification criteria, using the COT retrievals from Case A, GOES-17 cloud phase and CTP products.

Figure 10 shows the time-dependent COT and CER relative retrieval errors from each high cloud type shown in Table 2. In Figure 10a, the relative errors of COTs from cumulonimbus clouds have little dependence on LT, they remain at about 2.5% as the LT changes. However, in Figure 10a, the maximum of the COT relative errors from cirrus and cirrostratus clouds reach around 10% and 7.5%, respectively, at 8:00 LT and 16:00 LT (Figure 10a), which could be due to a stronger partial cloud coverage effect and relatively larger cloud fractions of cirrus and cirrostratus clouds compared to cumulonimbus clouds. The large SZA that appears at these two LTs could indicate a cloud 3D effect which biases the COT retrieval results. This could be the reason that the COT relative errors of cirrus and cirrostratus clouds have two peaks, that occur in the morning and afternoon. The variation of the COT relative errors from all types of high clouds, shown in Figure 8a, have similar trends, which indicates that the COT retrieval biases caused by sub-sampling are mainly contributed by cirrus and cirrostratus clouds. For the CER retrieval biases shown in Figure 10b, cirrus clouds provide the largest relative error around 8:00 and 16:00 LT, which corresponds to the two peaks of the CER relative error seen in Figure 8b. The relative errors of the CER from cirrostratus and cumulonimbus clouds are close to zero, and show little variation with LT due to the orthogonal correlation between COT and CER. Therefore, the relative error of the CER is mainly attributed to cirrus clouds.

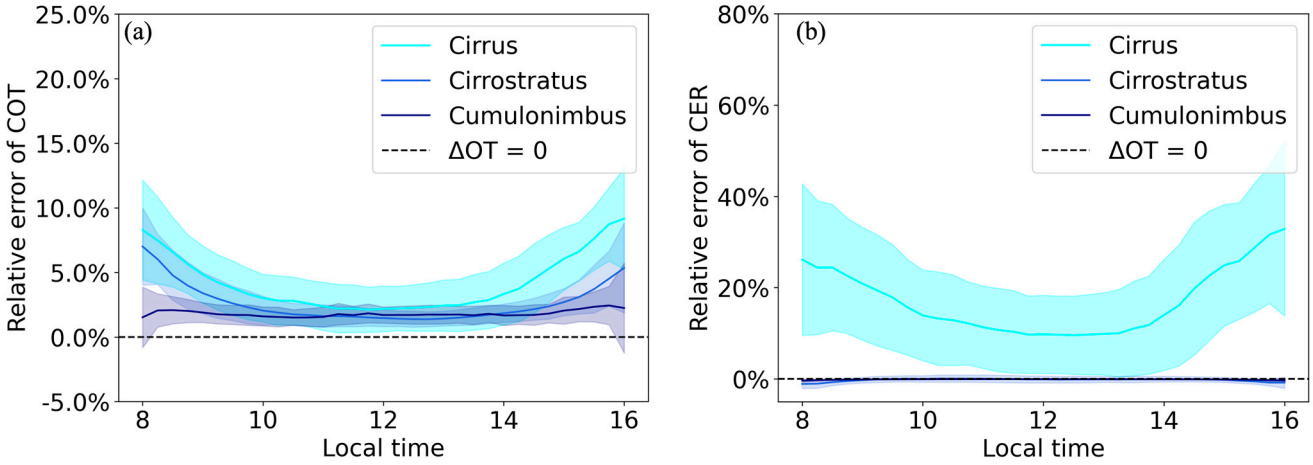

Figure 10. The contribution of each type of high cloud to the relative error of (**a**) COT and (**b**) CER retrievals as a function of LT with Case C sub-sampling.

4. Conclusions

This study investigates the COT and CER retrieval errors stemming from the resampling process by disentangling the effects associated with SZA, effective pixel resolution, cloud type, and temporal variation of the clouds' properties. It is found that larger uncertainties in the COT retrievals occur in Case C, that selects one 0.5-km pixel among 16 pixels, because one of the finest sub-pixels represents the reflectance of a super-pixel. The large relative errors for ice cloud COT retrievals with small or moderate COT values may be due to partial cloud coverage and a nonlinear relationship between COT and reflectance. For optically thick clouds, the relative errors may be attributed mainly to those clouds that have a small horizontal spatial scale. The high and positive CER relative errors, with a large uncertainty, appearing in the small CER cases (CER < 20 μm) are due to optically thin clouds that have positive COT relative errors and a nonorthogonal correlation between the COT and CER. The relative error of CER becomes negative as the CER becomes large (CER > 60 μm), which could be induced by the boundary limitation set in the retrieval system.

The distribution of the effective pixel resolution has been calculated, to investigate its impact on the retrieval result in the resampling process. The resolution of a sub-pixel or super-pixel is comparable to the horizontal spatial scale of most clouds when the effective pixel resolution of sub-pixels is small, which increases the partial cloud coverage effect. As a result, the relative errors of COT from cirrus and cirrostratus clouds decrease as the effective pixel resolution becomes coarser, due to increasing the probability of partly cloudy sub-pixels and super-pixels, which can weaken the impact from partial cloud coverage. The relative errors of the COT and CER from cirrus clouds display a strong correlation due to the nonorthogonal relationship between the COT and CER for cirrus clouds that have a small COT. Since the correlation between COT and CER is almost orthogonal when the COT is relatively large, the relative error of CER is close to 0 for cirrostratus and cumulonimbus clouds.

The relative biases of COT retrievals in ice clouds have a maximum value at 8:00 and 16:00 LT, and a minimum value around 12:00 LT, which is similar to the trend of the COT relative error derived from cirrus and cirrostratus clouds. Therefore, the biases are mainly caused by cirrus and cirrostratus clouds that are strongly affected by a partial cloud coverage effect, and have larger cloud fractions among all high cloud types, and thus larger probabilities of a cloud 3D effect. The relative error of the CER from cirrostratus and cumulonimbus clouds shows a weak LT dependence. The CER relative error shows two peaks, at 8:00 and 16:00 LT, which is attributed to cirrus clouds that are more sensitive to the change in the COT due to the nonorthogonal relationship between the COT and CER.

The potential biases associated with the sub-sampling process not only exist in COT and CER operational products, but also in other GOES-R series ABI operational products,

such as the cloud mask products that are similarly based on sub-sampled reflectance data. This study also indicates the impact of pixel resolution on the retrieval bias, which can provide insights about cloud inhomogeneity and partial cloud coverage effects for other satellite instruments that have varying spatial resolutions, such as MODIS, Visible Infrared Imaging Radiometer Suite (VIIRS), and Multi-angle Imaging Spectroradiometer (MISR). Furthermore, this study implies potential systematic biases in climatologies of cloud properties obtained from polar-orbiting satellites, that have infrequent overpasses of any one location, due to the time-dependence of cloud types and properties [45].

Author Contributions: Conceptualization, D.L., M.S. and P.Y.; methodology, D.L. and M.S.; software, D.L. and M.S.; validation, D.L. and M.S.; data curation, D.L.; Writing-Original draft preparation, D.L.; Writing-Review and Editing, D.L., M.S. and P.Y; visualization, D.L.; supervision, M.S. and P.Y. All authors have read and agreed to the published version of the manuscript.

Funding: This work was supported by Texas A&M University internal funds (account 132532-00095) and partly by endowment funds related to the David Bullock Harris Chair in Geosciences at the College of Geosciences, Texas A&M University (grant number 02-512231-0001).

Data Availability Statement: The GOES-17 ABI full disk operational products are freely available from NOAA CLASS (https://www.avl.class.noaa.gov/saa/products/search?sub_id=0&datatype_family=GRABIPRD&submit.x=21&submit.y=7 (accessed on 7 February 2022)).

Acknowledgments: The authors are grateful to the three anonymous reviewers who helped improve the quality of the manuscript. We would also like to thank the NOAA Comprehensive Large Array-data Stewardship System (CLASS) for providing GOES-R series ABI products. The numerical computations were conducted with high performance computation resources provided by Texas A&M University (http://hprc.tamu.edu (accessed on 8 April 2022)).

Conflicts of Interest: The authors declare no conflict of interest.

References

1. Hong, Y.; Liu, G.; Li, J.L.F. Assessing the Radiative Effects of Global Ice Clouds Based on CloudSat and CALIPSO Measurements. *J. Clim.* **2016**, *29*, 7651–7674. [CrossRef]
2. Baran, A.J. A Review of the Light Scattering Properties of Cirrus. *J. Quant. Spectrosc. Radiat. Transf.* **2009**, *110*, 1239–1260. [CrossRef]
3. Liou, K.-N.; Yang, P. *Light Scattering by Ice Crystals: Fundamentals and Applications*; Cambridge University Press: Cambridge, UK, 2016; ISBN 1316712443.
4. Kahn, B.H.; Takahashi, H.; Stephens, G.L.; Yue, Q.; Delanoë, J.; Manipon, G.; Manning, E.M.; Heymsfield, A.J. Ice Cloud Microphysical Trends Observed by the Atmospheric Infrared Sounder. *Atmos. Chem. Phys.* **2018**, *18*, 10715–10739. [CrossRef]
5. Gong, J.; Zeng, X.; Wu, D.L.; Li, X. Diurnal Variation of Tropical Ice Cloud Microphysics: Evidence from Global Precipitation Measurement Microwave Imager Polarimetric Measurements. *Geophys. Res. Lett.* **2018**, *45*, 1185–1193. [CrossRef] [PubMed]
6. Jiang, J.H.; Su, H.; Zhai, C.; Perun, V.S.; Del Genio, A.; Nazarenko, L.S.; Donner, L.J.; Horowitz, L.; Seman, C.; Cole, J.; et al. Evaluation of Cloud and Water Vapor Simulations in CMIP5 Climate Models Using NASA "A-Train" Satellite Observations. *J. Geophys. Res. Atmos.* **2012**, *117*. [CrossRef]
7. Várnai, T.; Marshak, A. Statistical Analysis of the Uncertainties in Cloud Optical Depth Retrievals Caused by Three-Dimensional Radiative Effects. *J. Atmos. Sci.* **2001**, *58*, 1540–1548. [CrossRef]
8. Platnick, S.; Meyer, K.G.; King, M.D.; Wind, G.; Amarasinghe, N.; Marchant, B.; Arnold, G.T.; Zhang, Z.; Hubanks, P.A.; Holz, R.E.; et al. The MODIS Cloud Optical and Microphysical Products: Collection 6 Updates and Examples from Terra and Aqua. *IEEE Trans. Geosci. Remote Sens.* **2017**, *55*, 502–525. [CrossRef]
9. Mace, G.G.; Zhang, Q. The CloudSat Radar-lidar Geometrical Profile Product (RL-GeoProf): Updates, Improvements, and Selected Results. *J. Geophys. Res. Atmos.* **2014**, *119*, 9441–9462. [CrossRef]
10. Saito, M.; Yang, P.; Hu, Y.; Liu, X.; Loeb, N.; Smith, W.L., Jr.; Minnis, P. An Efficient Method for Microphysical Property Retrievals in Vertically Inhomogeneous Marine Water Clouds Using MODIS-CloudSat Measurements. *J. Geophys. Res. Atmos.* **2019**, *124*, 2174–2193. [CrossRef]
11. Iwabuchi, H.; Putri, N.S.; Saito, M.; Tokoro, Y.; Sekiguchi, M.; Yang, P.; Baum, B.A. Cloud Property Retrieval from Multiband Infrared Measurements by Himawari-8. *J. Meteorol. Soc. Jpn. Ser. II* **2018**, *96B*, 27–42. [CrossRef]
12. Schmit, T.J.; Griffith, P.; Gunshor, M.M.; Daniels, J.M.; Goodman, S.J.; Lebair, W.J. A Closer Look at the ABI on the Goes-r Series. *Bull. Am. Meteorol. Soc.* **2017**, *98*, 681–698. [CrossRef]
13. Liu, Q.; Li, Y.; Yu, M.; Chiu, L.S.; Hao, X.; Duffy, D.Q.; Yang, C. Daytime Rainy Cloud Detection and Convective Precipitation Delineation Based on a Deep Neural Network Method Using GOES-16 ABI Images. *Remote Sens.* **2019**, *11*, 2555. [CrossRef]

14. Jiménez, P.A. Assessment of the GOES-16 Clear Sky Mask Product over the Contiguous USA Using CALIPSO Retrievals. *Remote Sens.* **2020**, *12*, 1630. [CrossRef]
15. Kristiansen, J.; Kristjánsson, J.E. Shortwave Cloud Forcing of Marine Stratocumulus Clouds. *Phys. Chem. Earth Part B Hydrol. Ocean. Atmos.* **1999**, *24*, 225–230. [CrossRef]
16. Haywood, J.M.; Osborne, S.R.; Abel, S.J. The Effect of Overlying Absorbing Aerosol Layers on Remote Sensing Retrievals of Cloud Effective Radius and Cloud Optical Depth. *Q. J. R. Meteorol. Soc.* **2004**, *130*, 779–800. [CrossRef]
17. Nakajima, T.; King, M.D. Determination of the Optical Thickness and Effective Particle Radius of Clouds from Reflected Solar Radiation Measurements. Part I: Theory. *J. Atmos. Sci.* **1990**, *47*, 1878–1893. [CrossRef]
18. Schmit, T.; Gunshor, M.; Fu, G.; Rink, T.; Bah, K.; Zhang, W.; Wolf, W.; Technology, R. Technology, R. GOES-R ABI Cloud and Moisture Imagery Product (CMIP) Algorithm Theoretical Basis Document. 2012, 1–63. Available online: https://www.star.nesdis.noaa.gov/goesr/documents/ATBDs/Baseline/ATBD_GOES-R_ABI_CMI_KPP_v3.0_July2012.pdf (accessed on 31 January 2023).
19. Coakley, J.A.; Friedman, M.A.; Tahnk, W.R. Retrieval of Cloud Properties for Partly Cloudy Imager Pixels. *J. Atmos. Ocean. Technol.* **2005**, *22*, 3–17. [CrossRef]
20. Zinner, T.; Mayer, B. Remote Sensing of Stratocumulus Clouds: Uncertainties and Biases Due to Inhomogeneity. *J. Geophys. Res. Atmos.* **2006**, *111*. [CrossRef]
21. Zhang, Z.; Werner, F.; Cho, H.; Wind, G.; Platnick, S.; Ackerman, A.S.; Di Girolamo, L.; Marshak, A.; Meyer, K. A Framework Based on 2-D Taylor Expansion for Quantifying the Impacts of Subpixel Reflectance Variance and Covariance on Cloud Optical Thickness and Effective Radius Retrievals Based on the Bispectral Method. *J. Geophys. Res. Atmos.* **2016**, *121*, 7007–7025. [CrossRef]
22. Werner, F.; Zhang, Z.; Wind, G.; Miller, D.J.; Platnick, S. Quantifying the Impacts of Subpixel Reflectance Variability on Cloud Optical Thickness and Effective Radius Retrievals Based On High-Resolution ASTER Observations. *J. Geophys. Res. Atmos.* **2018**, *123*, 4239–4258. [CrossRef]
23. Kahn, B.H.; Schreier, M.M.; Yue, Q.; Fetzer, E.J.; Irion, F.W.; Platnick, S.; Wang, C.; Nasiri, S.L.; L'Ecuyer, T.S. Pixel-scale Assessment and Uncertainty Analysis of AIRS and MODIS Ice Cloud Optical Thickness and Effective Radius. *J. Geophys. Res. Atmos.* **2015**, *120*, 11–669. [CrossRef]
24. Kato, S.; Marshak, A. Solar Zenith and Viewing Geometry-Dependent Errors in Satellite Retrieved Cloud Optical Thickness: Marine Stratocumulus Case. *J. Geophys. Res. Atmos.* **2009**, *114*, 1–13. [CrossRef]
25. Feind, R.E.; Christopher, S.A.; Welch, R.M. The Effect of Spatial Resolution upon Cloud Optical Property Retrievals. I-Optical Thickness. In Proceedings of the 12th Annual International Geoscience and Remote Sensing Symposium, Houston, TX, USA, 26–29 May 1992; Institute of Electrical and Electronics Engineers, Inc.: Piscataway, NJ, USA, 1992; Volume 1.
26. Henderson, B.G.; Chylek, P. The Effect of Spatial Resolution on Satellite Aerosol Optical Depth Retrieval. *IEEE Trans. Geosci. Remote Sens.* **2005**, *43*, 1984–1990. [CrossRef]
27. Heidinger, A. ABI Cloud Height Algorithm Theoretical Basis Document. 2010, 1–67. Available online: https://atmosphere-imager.gsfc.nasa.gov/sites/default/files/ModAtmo/MOD06-ATBD_2015_05_01_1.pdf (accessed on 31 January 2023).
28. Pavolonis, M. ABI Cloud Type and Cloud Phase Algorithm Theoretical Basis Document. 2010, 1–60. Available online: https://www.star.nesdis.noaa.gov/JPSS/documents/ATBD/ATBD_EPS_Cloud_CldType_v3.0.pdf (accessed on 31 January 2023).
29. Yang, P.; Hioki, S.; Saito, M.; Kuo, C.P.; Baum, B.A.; Liou, K.N. A Review of Ice Cloud Optical Property Models for Passive Satellite Remote Sensing. *Atmosphere* **2018**, *9*, 499. [CrossRef]
30. Yang, P.; Bi, L.; Baum, B.A.; Liou, K.-N.; Kattawar, G.W.; Mishchenko, M.I.; Cole, B. Spectrally Consistent Scattering, Absorption, and Polarization Properties of Atmospheric Ice Crystals at Wavelengths from 0.2 to 100 μM. *J. Atmos. Sci.* **2013**, *70*, 330–347. [CrossRef]
31. Saito, M.; Yang, P. Generalization of Atmospheric Nonspherical Particle Size: Interconversions of Size Distributions and Optical Equivalence. *J. Atmos. Sci.* **2022**, *79*, 3333–3349. [CrossRef]
32. Huang, X.; Yang, P.; Kattawar, G.; Liou, K.-N. Effect of Mineral Dust Aerosol Aspect Ratio on Polarized Reflectance. *J. Quant. Spectrosc. Radiat. Transf.* **2015**, *151*, 97–109. [CrossRef]
33. Rodgers, C.D. *Inverse Methods for Atmospheric Sounding: Theory and Practice*; World Scientific: Singapore, 2000; Volume 2, ISBN 9814498688.
34. Heidinger, A.; Straka, W.C. ABI Cloud Mask Algorithm Theoretical Basis Document. 2013, 1–106. Available online: https://www.star.nesdis.noaa.gov/goesr/documents/ATBDs/Baseline/ATBD_GOES-R_Cloud%20Height_v3.0_July%202012.pdf (accessed on 31 January 2023).
35. Dong, X. The Impact of Surface Albedo on the Retrievals of Low-Level Stratus Cloud Properties: An Updated Parameterization. *Geophys. Res. Lett.* **2005**, *32*, 1–4. [CrossRef]
36. Cho, H.; Zhang, Z.; Meyer, K.; Lebsock, M.; Platnick, S.; Ackerman, A.S.; Di Girolamo, L.; C.-Labonnote, L.; Cornet, C.; Riedi, J. Frequency and Causes of Failed MODIS Cloud Property Retrievals for Liquid Phase Clouds over Global Oceans. *J. Geophys. Res. Atmos.* **2015**, *120*, 4132–4154. [CrossRef]
37. Hioki, S.; Yang, P.; Baum, B.A.; Platnick, S.; Meyer, K.G.; King, M.D.; Riedi, J. Degree of Ice Particle Surface Roughness Inferred from Polarimetric Observations. *Atmos. Chem. Phys.* **2016**, *16*, 7545–7558. [CrossRef]
38. Rossow, W.B.; Schiffer, R.A. ISCCP Cloud Data Products. *Bull. Am. Meteorol. Soc.* **1991**, *72*, 2–20. [CrossRef]

39. Cornet, C.; Labonnote, L.C.; Waquet, F.; Szczap, F.; Deaconu, L.; Parol, F.; Vanbauce, C.; Thieuleux, F.; Riédi, J. Cloud Heterogeneity on Cloud and Aerosol above Cloud Properties Retrieved from Simulated Total and Polarized Reflectances. *Atmos. Meas. Tech.* **2018**, *11*, 3627–3643. [CrossRef]
40. King, M.D.; Tsay, S.-C.; Platnick, S.E.; Wang, M.; Liou, K.-N. Cloud Retrieval Algorithms for MODIS: Optical Thickness, Effective Particle Radius, and Thermodynamic Phase. *MODIS Algorithm Theor. Basis Doc.* **1997**, *1997*, 1–79.
41. Fu, R.; Del Genio, A.D.; Rossow, W.B. Behavior of Deep Convective Clouds in the Tropical Pacific Deduced from ISCCP Radiances. *J. Clim.* **1990**, *3*, 1129–1152. [CrossRef]
42. Wood, R.; Field, P.R. The Distribution of Cloud Horizontal Sizes. *J. Clim.* **2011**, *24*, 4800–4816. [CrossRef]
43. Iwabuchi, H.; Hayasaka, T. Effects of Cloud Horizontal Inhomogeneity on the Optical Thickness Retrieved from Moderate-Resolution Satellite Data. *J. Atmos. Sci.* **2002**, *59*, 2227–2242. [CrossRef]
44. Teng, S.; Liu, C.; Zhang, Z.; Wang, Y.; Sohn, B.; Yung, Y.L. Retrieval of Ice-over-water Cloud Microphysical and Optical Properties Using Passive Radiometers. *Geophys. Res. Lett.* **2020**, *47*, e2020GL088941. [CrossRef]
45. Tselioudis, G.; Lacis, A.A.; Rind, D.; Rossow, W.B. Potential Effects of Cloud Optical Thickness on Climate Warming. *Nature* **1993**, *366*, 670–672. [CrossRef]